Onset of instability with collapse observed in relatively high density and medium beta regions of LHD

Onset of instability with collapse observed in relatively high density and medium beta regions of LHD

Yuki Takemura, Kiyomasa Watanabe, Satoru Sakakibara, et al.

View Online   Export Citation   CrossMark

ARTICLES YOU MAY BE INTERESTED IN

Physics of Plasmas

Special Topic: Plasma Physics of the Sun in Honor of Eugene Parker

Submit Today!

Onset of instability with collapse observed in relatively high density and medium beta regions of LHD

View Online   Export Citation   CrossMark

Yuki Takemura,[1,a] (iD) Kiyomasa Watanabe,[1,2] Satoru Sakakibara,[1,3] Satoshi Ohdachi,[1,4] Yoshiro Narushima,[1,3]
Kenji Tanaka,[1,5] and Tokihiko Tokuzawa[1,3] (iD)

AFFILIATIONS

[1]National Institute for Fusion Science, National Institutes of Natural Sciences, Toki, Gifu 509-5292, Japan
[2]Department of Energy Engineering, Graduate School of Engineering, Nagoya University, Nagoya, Aichi 464-8603, Japan
[3]The Graduate University for Advanced Studies, SOKENDAI, Toki, Gifu 509-5292, Japan
[4]Graduate School of Frontier Sciences, The University of Tokyo, Kashiwa, Chiba 277-8561, Japan
[5]Interdisciplinary Graduate School of Engineering Sciences, Kyushu University, Kasuga, Fukuoka 816-8580, Japan

[a]Author to whom correspondence should be addressed: takemura.yuki@nifs.ac.jp

ABSTRACT

Edge MHD instabilities with pressure collapse are found in relatively high beta and low magnetic Reynolds number regions with a magnetic axis torus outward-shifted configuration of the large helical device (LHD), and characteristics and onset conditions of the instability are investigated. The instability has a radial structure with an odd parity around the resonant surface, which is different from that of the interchange instability typically observed in the LHD. The onset condition dependence on the magnetic axis location shows that the onset beta increases as the magnetic axis location moves more torus inwardly, and the instability appears only in limited configurations where the magnetic axis is located between 3.65 and 3.775 m. In such configurations, the resonant surface location is close to an index of the plasma boundary. This fact suggests that the distance between the resonant surface location and the plasma boundary plays an important role in the onset, and a possibility that the instability is driven by an external mode.

I. INTRODUCTION
A. MHD instability with collapse in tokamaks and Large Helical Device (LHD)

In research to improve the performance of core plasmas in magnetic confinement fusion devices, an important subject is to suppress and avoid rapid degradation of the pressure gradient (collapse phenomena) caused by MHD instabilities. In tokamaks, disruptions caused by current-driven MHD instabilities are a major concern for stable operation.[1,2] In helical plasmas, where a plasma current is not required to form a magnetic field for plasma confinement, tokamak-like disruptions driven by current-driven instabilities can be avoided in principle, but collapse phenomena leading to the degradation of global confinement without terminating plasma discharges are sometimes caused by pressure-driven instabilities.

In the Large Helical Device (LHD),[3] one of the helical fusion experimental devices, various collapse phenomena have been observed,

depending on magnetic configurations such as in the torus major radial location of the magnetic axis (R_{ax}) and plasma aspect ratio, and plasma discharge conditions. In the magnetic axis torus inward-shifted configurations like $R_{ax} < 3.60$ m, where the magnetic hill is relatively high and magnetic shear is low, a collapse phenomenon is driven by $m/n = 2/1$ MHD instabilities, excited in the core region.[4] Here, m and n mean the poloidal and toroidal mode number, respectively. The magnetic hill is related to the average magnetic field line curvature, and the interchange mode is unstable in the magnetic hill regime. It should be noted that in a magnetic configuration with $R_{ax} = 3.60$ m, high beta discharges equivalent to fusion plasmas were obtained.[5] When a peaked pressure profile is formed in the magnetic configurations with $R_{ax} > 3.60$ m, a "core density collapse (CDC)" phenomenon is observed, which is considered to be driven by ballooning instabilities.[6,7] When magnetic shear is low in the toroidal plasma current carrying high aspect plasmas, locked-mode-like instabilities appear.[8–10]

B. Observation of edge instability with collapse in LHD

As noted above, the characteristics of MHD instabilities depend on MHD equilibrium. Figure 1 shows the radial profiles of (a) a rotational transform, (b) magnetic shear squared (stabilizing term of the Suydum criterion), and (c) a magnetic hill index (driving term) (see the Appendix), where V, s, B_0, R_0, $2\pi\Psi_e$, a_p, and r are plasma volume, normalized toroidal flux, the toroidal field at the magnetic axis, the major radius at the magnetic axis, the toroidal flux at the plasma boundary, the effective minor radius at the plasma boundary, and the effective minor radius, respectively. Here, the plasma boundary is defined by the last closed flux surface.[11] The equilibrium is calculated by the 3D MHD equilibrium calculation code , Variational Moments Equilibrium Code (VMEC).[12] In the configuration with $R_{ax} = 3.60$ m, the whole area of the radial profile is in the magnetic hill region. Magnetic shear is low in the core but high in the periphery. This paper focuses on the $m/n = 1/1$ resonant surface, which is located in the peripheral region. When R_{ax} is more outward than 3.60 m, the resonant surface location shifts more to the periphery, magnetic shear, and the magnetic hill index at the resonant surface increase (3.75 m

vacuum in Fig. 1). Nevertheless, the rate of reduction in the magnetic hill index is larger than that in magnetic shear. When beta increases, magnetic shear and the magnetic hill index at the resonant surface increase due to the Shafranov shift (3.75 m high beta in Fig. 1). In such a configuration, the instabilities with collapse having an $m/n = 1/1$ structure are observed. As shown in Sec. I C, the instabilities occur in the relatively high beta and low magnetic Reynolds number regime. On the other hand, the LHD discharges without collapse have been achieved in the regime of the volume-averaged beta value higher than the above onset value and lower S of $\sim10^5$.[13]

Figure 2 shows waveforms of a typical discharge where the instabilities with collapse occur in the $R_{ax} = 3.75$ m configuration. A plasma is produced and maintained by tangential neutral beam injections (NBIs) from $t = 1.3$ s [Fig. 2(a)]. The electron density increases from $t = 1.5$ to 2.0 s by hydrogen gas puffing [Fig. 2(b)]. At $t = 2.0$ s, the magnetic fluctuation grows rapidly [Fig. 2(d)]. At this time, despite constant heating power, beta value decreases by about 10% [Fig. 2(e)], which means a collapse occurs. Since the growth of the magnetic fluctuation is saturated, the disruption does not occur, but the beta degradation is maintained. It should be noted that the line-averaged electron density of an edge chord (3.40 m) of the far-infrared (FIR) laser interferometer is oscillated during the beta degradation, which suggests that the resonant surface is located at the edge [Fig. 2(c)]. At $t = 2.6$ s, magnetic fluctuation amplitude rapidly decreases, and beta
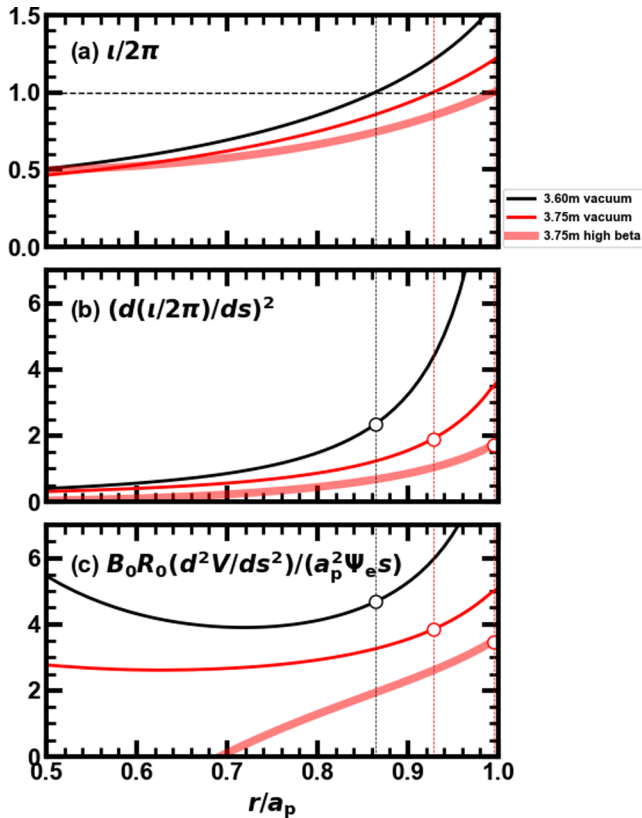

FIG. 1. MHD equilibrium characteristics of the LHD. Radial profiles of (a) rotational transform, (b) magnetic shear squared (stabilizing term of the Suydum criterion), and (c) magnetic hill index (driving term) with different configurations and conditions. Horizontal axis is the normalized minor radius. Equilibrium parameters are based on a hypothetical VMEC equilibrium under the assumption of beta value and its profile, no plasma current. The black/red lines correspond to a magnetic axis of 3.60/3.75 m in vacuum, and the thick red line to a magnetic axis of 3.75 m at high beta, circles to parameters at $\iota/2\pi = 1$.

FIG. 2. Waveforms of typical discharge where the instability with collapse occurs in the $R_{ax} = 3.75$ m configuration: (a) total heating power of NBIs, (b) core line-averaged electron density, (c) line-averaged electron density of edge chords of the FIR interferometer, (d) a magnetic fluctuation due to the instability, (e) volume-averaged beta value, and (f) plasma current normalized by toroidal magnetic field strength at the magnetic axis.

value returns to that before the instability occurs. This result suggests that beta value is clearly limited by the instability.

Figure 3(a) shows radial profiles of the rotational transform. It should be noted that rotational transforms are evaluated based on VMEC calculations, assuming no plasma current. Figures 3(b), 3(c), and 3(d) show local electron temperature, density, and pressure measured by the Thomson scattering system before (in blue) and after (in red) the onset of the instability, respectively. The shape of the electron pressure profile is similar to that of the electron temperature profile because the electron density profile is roughly flat over a wide region. After the onset, the electron pressure gradient is reduced near the resonant surface of the instability, and the reduced gradient drives the pressure reduction over a broad region inside the resonant surface, which leads to the degradation of the volume-averaged beta value.

C. Onset conditions of edge instability with collapse

Figure 4 shows onset parameters of the instability in the $R_{ax} = 3.75$ m configuration with a different toroidal magnetic field strength at the magnetic axis, B_t. Here, the positive and negative B_t corresponds to the clockwise and counterclockwise direction, respectively. Closed and open circles correspond to parameters before and at the onsets, respectively. When electron density and beta value reach a specific region, the instabilities appear. The onset density is 4.5×10^{19} m^{-3} at $B_t = -0.75$ T and 3.0×10^{19} m^{-3} at -0.60 T, and the onset

FIG. 4. Onset regime of the instability with collapse in the $R_{ax} = 3.75$ m configuration in the diagram of beta value and (a) line-averaged electron density and (b) magnetic Reynolds number, S. Filled (open) circles correspond to parameters before (at) the onset of the instability. Red (blue) symbols correspond to parameters at $B_t = -0.75$ T (-0.60 T) and a red line to time evolution of parameters in the #154036 discharge, as shown in Fig. 5. A black bold line shows the onset conditions of parameters.

beta value is 1.45% at -0.75 T and 1.60% at -0.60 T [Fig. 4(a)]. Figure 4(b) shows the onset regime in the diagram of beta value and the magnetic Reynolds number at the resonant surface, S. Here, S is defined as τ_r/τ_a, and τ_r and τ_a are the resistive diffusion time and the Alfvén time, respectively. As indicated by a black bold line in Fig. 4(b), the onset conditions look the same despite different B_t. The red line in Fig. 4(b) corresponds to the time evolution of parameters in the discharges of Fig. 5. At the beginning of the discharge, beta value is relatively low, and S is high; then, beta value increases and S decreases as electron density increases. Eventually, when the beta value and S satisfy the onset conditions, the instabilities appear. This result suggests that beta value and S are key parameters for the instability to occur.

In this study, typical characteristics and onset conditions of the instability with collapse were investigated experimentally in the LHD. This paper is organized as follows: In Sec. II, the diagnostics to detect the instability with collapse are introduced. In Sec. III, typical characteristics of the instability like the frequency spectrum and spatial structures of the instability are shown. In Sec. IV, magnetic configuration dependence of the onset conditions and a discussion about the driving mechanism are reported. In Sec. V, collapse events observed in the LHD are explained and positioning of the instability reported in this paper within them is described. A summary and
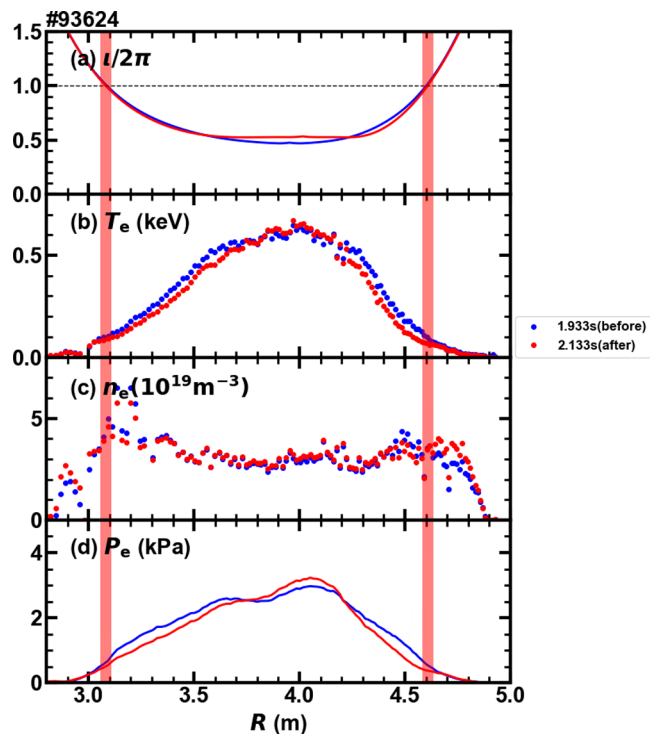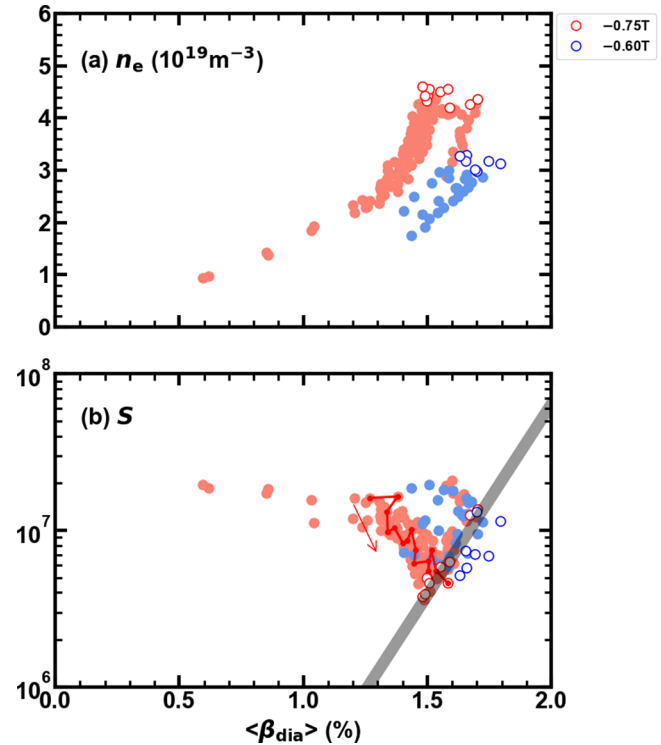

FIG. 3. Radial profiles of (a) rotational transform, (b) local electron temperature, (c) local electron density, and (d) local electron pressure before (in blue) and at the onset of the instability (in red). Note that the iota profiles are not based on measured pressure profile and current profile, but is only reference data. The red-filled area corresponds to $\iota/2\pi = 1$ after the onset.
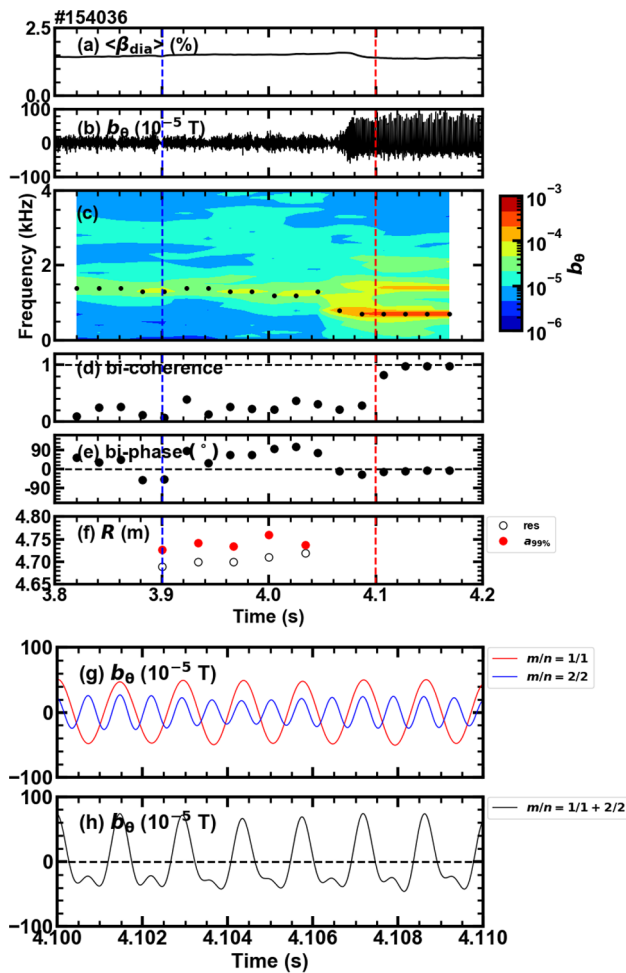
FIG. 5. Magnetic fluctuation characteristics of the instability with collapse in the $R_{ax} = 3.75$ m configuration. (a) Volume-averaged beta value, (b) a magnetic fluctuation, (c) amplitude spectrum of the magnetic fluctuation and frequency of a peak amplitude component in the spectrum (f_{peak}, black circles), (d) bi-coherence between three waves with $(m, n, f) = (1, 1, f_{peak})$, $(1, 1, f_{peak})$, and $(2, 2, 2f_{peak})$, (e) bi-phase and (f) the location of the resonant surface and that of $a_{99\%}$. Figures (g) and (h) show the $m/n = 1/1$ and 2/2 magnetic fluctuations and the composite wave during the appearance of the instability, respectively. Vertical lines correspond to the timings of the radial mode structure shown in Figs. 7(d2) and 7(d3).

conclusions are presented in Sec. VI. In the Appendix, a stability index for the ideal interchange instability is considered.

II. DIAGNOSTICS TO DETECT INSTABILITY

The poloidal and toroidal structures of the instability with collapse were measured by using magnetic probe arrays outside a plasma.[14] The radial profiles of local electron temperature, density, and pressure were measured by a Thomson scattering system with a time interval of 33 ms. The measurement spots were located at both torus-inboard and outboard sides in the equatorial plane of the horizontal-elongated cross section. The radial mode structure was measured by a CO_2 laser interferometer.[15] Note that the Thomson scattering system had poor time resolution for MHD instability

detection, and the electron cyclotron emission measurement was unavailable because of low $|B_t|$, at which the instability appeared. The interferometer chords were located in the almost vertically elongated cross section. In order to detect fast changes of core pressure, soft x-ray intensity was measured by soft x-ray detector arrays. Their measurement chords were located at both torus-inboard and outboard sides in the vertically elongated cross section. Poloidal plasma flow fluctuation related to the instability was measured by using a micro-wave Doppler reflectometer.[16] The measurement spots were located at the torus-outboard side in the equatorial plane of the horizontally elongated cross section.

III. TYPICAL CHARACTERISTICS OF INSTABILITY

Figure 5 shows the magnetic fluctuation characteristics of the instability with collapse in the $R_{ax} = 3.75$ m configuration. The onset time of the instability is $t \sim 4.08$ s, when the growth of the instability and degradation of the global confinement occurs [Figs. 5(a) and 5(b)]. Before the onset, the magnetic fluctuation has an $m/n = 1/1$ structure, as the dominant frequency component in the 1.5 kHz band, and a 2/2 structure as the frequency component in the 3 kHz band. They are estimated to be resistive interchange instabilities, which are typically observed at the LHD.[13] After the onset, the magnetic fluctuation has a 1/1 structure, as the dominant frequency component in the 700 Hz band, and a 2/2 structure as the frequency component in the 1.5 kHz band. Frequency of the 1/1 fluctuation, f_{peak}, is clearly smaller than the above typical frequency, and the 1/1 fluctuation amplitude is about three times larger than that before the onset. Figures 5(d) and 5(e) show bi-coherence and bi-phase[17] between three waves with $(m, n, f) = (1, 1, f_{peak})$, $(1, 1, f_{peak})$, and $(2, 2, 2f_{peak})$. After the onset, bi-coherence becomes very high, and bi-phase is $\sim 0°$. High bi-coherence suggests that the 1/1 and 2/2 fluctuations after the onset are likely to be derived from one mode (so-called high harmonic mode), which means that both fluctuations are derived from the same source. Figures 5(g) and 5(h) show the 1/1 and 2/2 fluctuations and their composite wave. The median of the composite wave is shifted from zero.

Now the reason for the formation of the above 1/1 and 2/2 fluctuations after the onset is discussed. Figure 6 shows the Fourier spectrum of plasma flow velocity, measured by a microwave Doppler reflectometer during an appearance of the instability. Figure 6(a) displays the frequency, f_p, evaluated from flow velocity normalized by the characteristic length. The constant component of f_p is about 900 Hz [Fig. 6(a)], which is similar to the frequency of the instability (~ 700 Hz). The dominant frequency component of the instability in the 700 Hz band has high coherence between f_p and a magnetic fluctuation, as shown in Fig. 6(b), which suggests that plasma flow is fluctuated at the frequency of the instability. It is found that the amplitude of f_p fluctuation is ~ 200 Hz. If a magnetic fluctuation is simply expressed as $\sin(\varphi)$ based on flow fluctuation, $\varphi = \int (2\pi f(t)) dt$ and $f(t) = \delta f \times \sin(2\pi f_0 t)$, where f_0 and δf are the amplitude of a constant component and that of the dominant frequency component, respectively. As δf is increased, the waveform of the magnetic fluctuation is distorted, resulting in formation of the higher harmonics. As already explained above, the instability with collapse has higher harmonic components, which can be attributed to large flow fluctuation due to the instability.

Figure 5(f) shows time evolution of the torus major radius in a horizontally elongated cross section of the flux surface on the mid-plane of the outboard side at $\iota/2\pi = 1$, R_{res}, and at an index of the
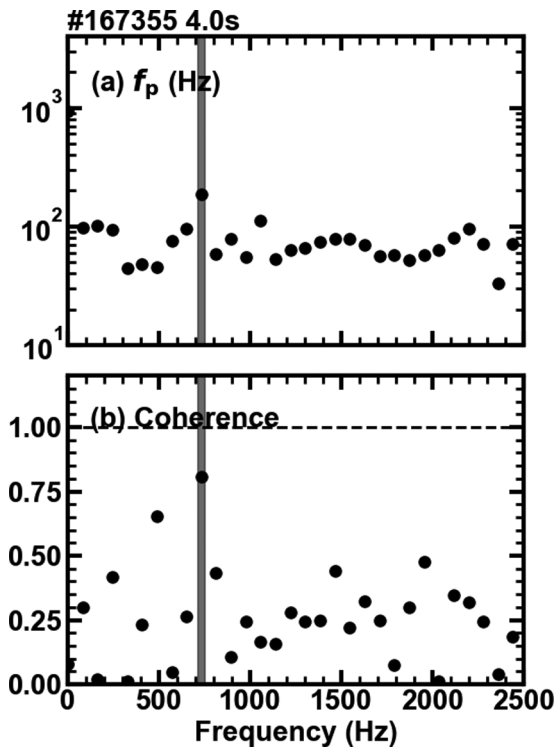
FIG. 6. Fourier spectra of the plasma flow velocity signal during the appearance of the instability: (a) the flow velocity fluctuation amplitude normalized by the characteristics length and (b) coherence between the flow fluctuation and the magnetic fluctuation. Vertical line corresponds to a high coherent component.

plasma boundary, $R_{a99\%}$ (at the effective minor radius containing 99% of the volume-averaged value of the electron pressure[18]). The value of R_{res} is estimated from the central position of the flat region in the electron pressure profile, because the flattening occurs due to the instability. Before the onset, $R_{a99\%}$ is largely unchanged, but R_{res} moves to the periphery with time. This shift of R_{res} can be attributed to the Shafranov shift, due to the finite beta effect and the change in the current profile. It is found that at the onset, R_{res} is located quite close to $R_{a99\%}$.

Figure 7 shows the radial structures of $m/n = 1/1$ line-integrated electron density fluctuations, measured by the CO_2 laser interferometer. The interferometer has many sight lines densely around the periphery, where $\iota/2\pi = 1$ surface is located [Fig. 7(a)]. Figures 7(c1)–7(c3) and 7(d1)–7(d3) show the amplitude of line-averaged electron density fluctuations and the phase difference between them and a magnetic fluctuation, respectively. Before the onset ($t = 3.60$ s), the phase differences in the high coherent region are almost constant. This is an even-function type structure, which is similar to the radial structure of interchange modes. At $t = 3.90$ s, where the density is higher than at $t = 3.60$ s, the phase difference between two peaks ($R \sim 4.18$ and 4.20 m) of the fluctuation amplitude is not constant. This suggests a possibility that a rotating magnetic island of narrow width appears, but its identification is a future work. On the other hand, after the onset ($t = 4.10$ s), the amplitude profile has two peaks and the phase difference between them is different by about 90°.

This result suggests that the mode has the radial structure with an odd parity, which is similar to that of the tearing modes [Figs. 7(d3) and 7(e3)]. Note, however, that the phase difference between the two peaks is not 180°, which would be due to the line-integrated effect of the measurement. The core line-averaged electron density measured by the FIR laser interferometer is 2.5×10^{19} m^{-3} at $t = 3.60$ s, 3.9×10^{19} m^{-3} at 3.90 s, and 4.5×10^{19} m^{-3} at 4.10 s. Therefore, the marginal density region, where the phase structure is changed, is $\sim 3.9 \times 10^{19}$ m^{-3}.

Figure 8 shows the process of the appearance and disappearance of the instability during a discharge. In the appearance process, the amplitude of the magnetic fluctuation increases and its frequency decreases [Figs. 8(c) and 8(d)]. The growth rate of the fluctuation is ~ 90 Hz (11 ms). From the middle of growth of the fluctuation, the volume-averaged beta value begins to fall and decreases more slowly than the growth rate of the fluctuation. When the fluctuation amplitude approaches its saturation level, the core soft x-ray intensity decreases in ~ 2 ms [red line in Fig. 8(e)]. Eventually, beta value and core soft x-ray intensity become constant. The sequence of the processes (growth of the fluctuation, rapid decrease in core soft x-ray intensity, and slow decrease in beta value) suggests that at a specific time, the pressure gradient rapidly decreases (e.g., due to the transport in the magnetic field direction) due to growing instabilities, which leads to saturation of the instabilities. In the disappearance process, suppression of the fluctuation and an increase in frequency occur [Figs. 8(h) and 8(i)]. The suppression time of the fluctuation is ~ 3 ms. Beta value and core soft x-ray intensity increase slowly [Figs. 8(f) and 8(j)]. Eventually, beta value is recovered to that before the appearance of the instability. The sequence of the processes (suppression of the fluctuation, slow increase in core soft x-ray intensity and beta value) suggests that the pressure gradient is gradually restored on the radial transport timescale as a result of suppression of the instability.

IV. MAGNETIC CONFIGURATION DEPENDENCE OF ONSET CONDITION OF INSTABILITY AND DISCUSSION OF ONSET MECHANISM

Figure 9 shows the onset conditions with various R_{ax} configurations in the diagram of beta value and the magnetic Reynolds number, S. The onset beta and the onset S for the $R_{ax} = 3.75$ m configuration are the same as those shown in Fig. 4(b). The instability occurs only in configurations with $R_{ax} = 3.65$–3.775 m. When the R_{ax} decreases, the onset beta value increases. The instability is more likely to occur at lower beta values when R_{ax} is larger. Assuming that the onset beta-S relationship for $R_{ax} = 3.70/3.65/3.60$ m is the same as that for 3.75 m, the beta value at a specific S for 3.70/3.65 m is evaluated based on observed onset parameters and that for 3.60 m is extrapolated from those for 3.65–3.775 m. The obtained condition for 3.75/3.70/3.65 m is shown as solid lines and that for 3.60 m as s dashed line of Fig. 9. Even if beta value and S satisfy the evaluated onset conditions for the 3.60 m configuration, the instability does not occur. Similarly for the 3.80 m configuration, even if beta value and S satisfy the onset conditions for the 3.75 m configuration, for which onset beta value is expected to be larger than that for the 3.80 m configuration, no instability is observed.

As shown in Fig. 5(f), $\iota/2\pi = 1$ surface in the torus major radial location (R_{res}) at the onset of the instability is located close to an index of the plasma boundary ($R_{a99\%}$), which is similar to the onset condition for the $m/n = 1/1$ external ideal interchange mode. The ideal stability analysis of 3D MHD simulations predicts that the external mode
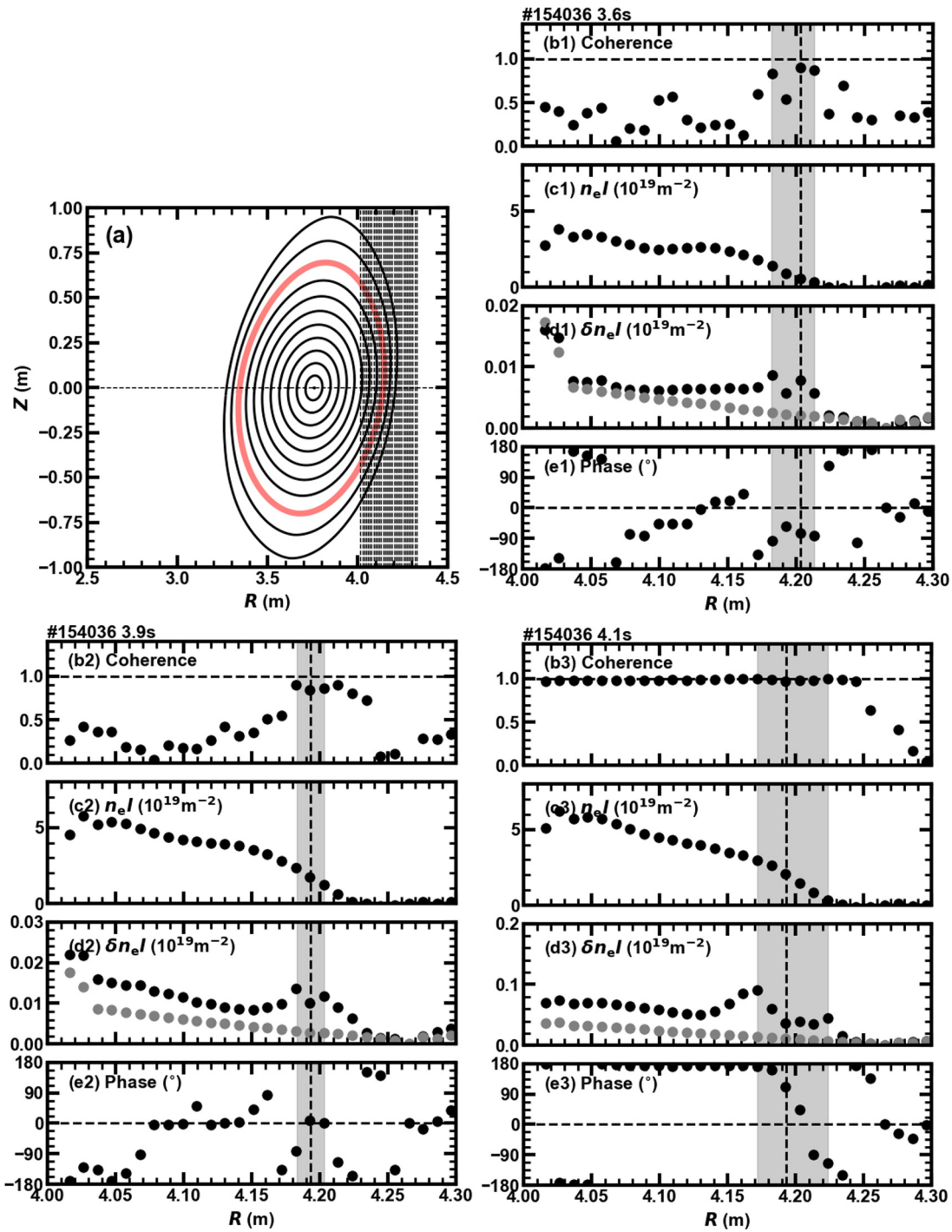
FIG. 7. The radial mode structure of $m/n = 1/1$ fluctuations. (a) Chords of CO_2 laser interferometer. The lines of the magnetic surface are shown every $r/a_p = 0.1$, and a red thick line corresponds to $r/a_p = 1$ in the vacuum configuration with $R_{ax} = 3.75$ m. (b) Coherence between line-averaged electron density fluctuations and a magnetic fluctuation, (c) time-averaged density signals, (d) amplitude of density fluctuations, and (e) phase difference between density fluctuations and a magnetic fluctuation before occurrence of the instability at 3.6 and 3.9 s, and during the appearance of the instability at 4.1 s. Gray symbols in the amplitude profiles correspond to the noise level. Hatched area in (b1)–(e1) corresponds to the high coherence region and vertical dashed line displays the peak location within the high coherence region. Hatched areas in (b2)–(e2) and (b3)–(e3) correspond to the region between two peaks, and vertical dashed lines display the location of valley between two peaks.
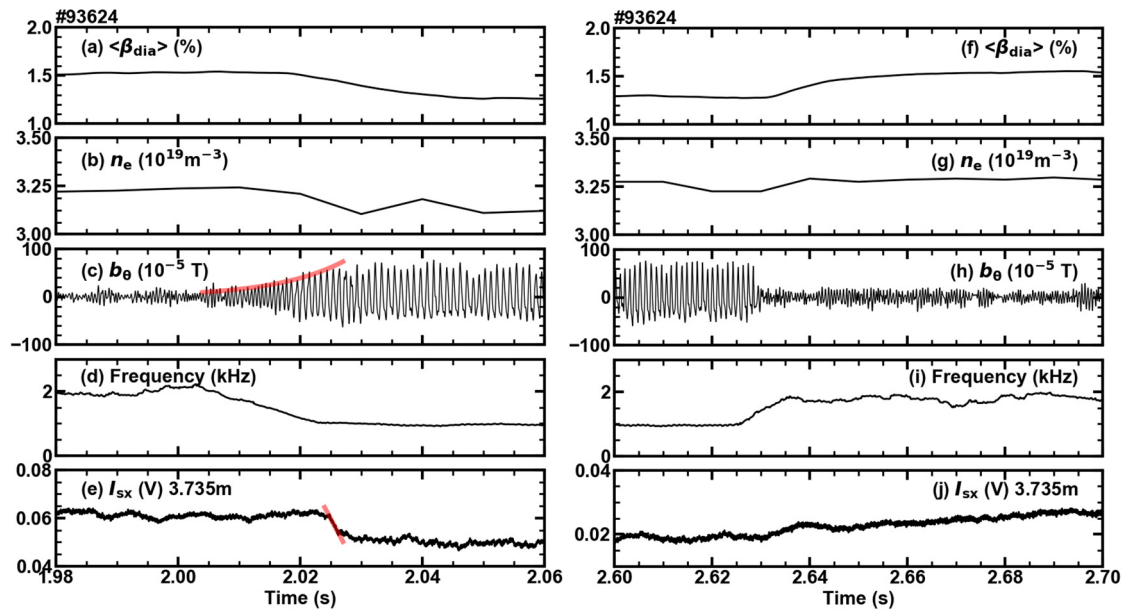
FIG. 8. (a)–(e) Appearance process and (f)–(j) disappearance process of the instability. (a) and (f) Volume-averaged beta value, (b) and (g) line-averaged electron density, (c) and (h) a magnetic fluctuation, (d) and (i) frequency of the instability, and (e) and (j) core soft x-ray intensity.

is unstable when $\iota/2\pi = 1$ surface is located slightly outside the plasma boundary.[19–21] Since the identification of the plasma boundary location is difficult in helical plasmas,[22] $R_{a99\%}$ is used as an indicator of the plasma boundary in the following analysis. Figure 10 shows the R_{ax} dependence of (a) R_{res}, (b) $R_{a99\%}$, and (c) their distances. The onset condition of distances is shaded in Fig. 10(c). Independently of R_{ax}, instabilities appear when the distances normalized by the plasma minor radius are around +5%, and the scatters of the onset condition are within 5%. On the contrary, in the $R_{ax} = 3.60$ m configuration, $R_{a99\%}$ is outside R_{res}, and in the $R_{ax} = 3.80$ m configuration, $R_{a99\%}$ is inside R_{res}. When the distances between R_{res} and $R_{a99\%}$ are outside the shaded area, the

instability does not appear. The distances between R_{res} and $R_{a99\%}$ are determined from the relationship between the Shafranov shift and the characteristics of the vacuum magnetic configuration, which would lead to the beta value dependence of the onset condition. On the other hand, the reason for the S dependence is still unclear.

The external modes predicted in papers[19–21] are derived from ideal-interchange instabilities, and the radial profile of the radial displacement is an even-function structure across the resonant surface, which differs from the observed radial displacement profile of the instabilities, as shown in Figs. 7(d3) and 7(e3). MHD instability analysis including finite resistivity in a 3D MHD equilibrium configuration is necessary to clarify the driving mechanism of the instability, but this is also one of the future subjects for study. The identification of effective plasma boundary conditions for external MHD instabilities is another future work.

Next, the effect of plasma current on the onset conditions of the instabilities is investigated: plasma current leads to the change in the $\iota/2\pi = 1$ resonant surface location and varies depending on the injection direction of tangential NBs. Figure 11 shows the onset conditions in the beta-S diagram for $R_{ax} = 3.75$ m and $B_t = -0.75$ T. The data were classified by evaluating the increment of the edge rotational transform due to plasma current. In the range of the obtained rotational transform, no influence on the onset condition appears. Future experiments with significantly different current profiles, such as long-pulse NBIs and switching the injection direction during the discharge, are required to investigate the effect of the current profile on the onset conditions.

V. POSITIONING OF INSTABILITY WITHIN COLLAPSE EVENTS OBSERVED IN LHD

This section summarizes the characteristics of the collapse phenomena observed in the LHD, in order to clarify the position of the
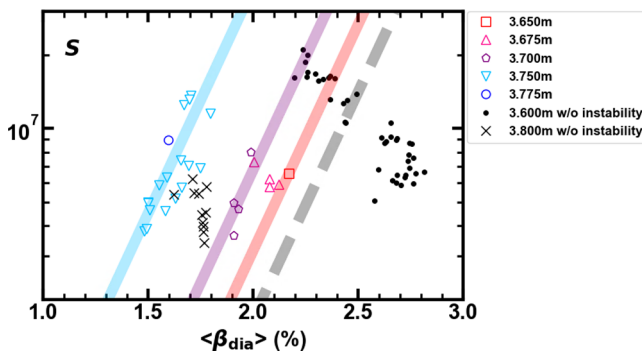

FIG. 9. Onset regime with various R_{ax} configuration in the diagram of beta value and magnetic Reynolds number, S. Parameters with $R_{ax} = 3.75$ m are the same as those at the onset, as shown in Fig. 4(b). The auxiliary lines (light blue/purple/red) display the onset conditions of beta and S with various R_{ax} (3.75/3.70/3.65 m), respectively. Each condition is evaluated from the onset condition with $R_{ax} = 3.75$ m and from R_{ax} dependence of the onset beta. The dashed line corresponds to the estimated onset condition with 3.60 m.

FIG. 11. Onset conditions of the instability with collapse in the diagram of beta value and the magnetic Reynolds number, S, for the various plasma current discharges with the $R_{ax} = 3.75$ m and $B_t = -0.75$ T. Here, the current effect is evaluated by the increment of the edge rotational transform due to the current.
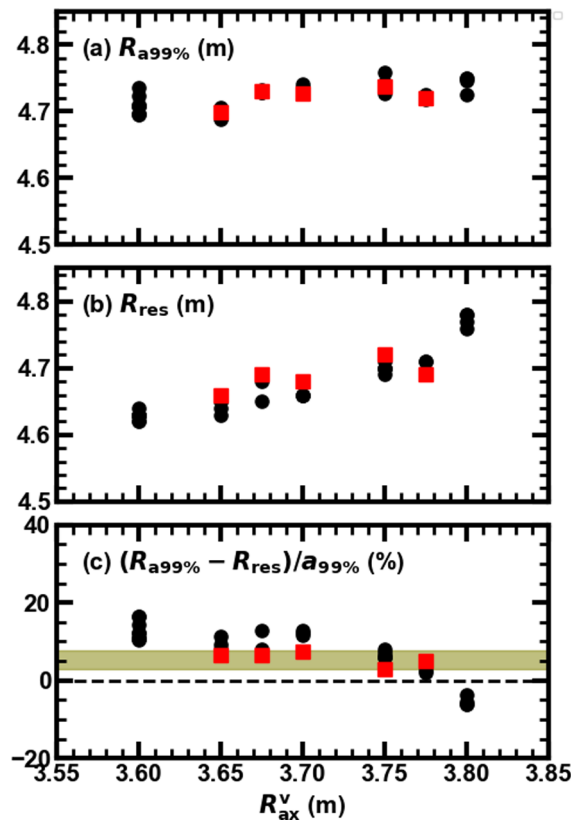

FIG. 10. The vacuum magnetic axis location dependence of (a) an index of the plasma boundary, $R_{a99\%}$, (b) the $m/n = 1/1$ resonant surface location, R_{res}, and (c) the distances between $R_{a99\%}$ and R_{res}. The square symbols correspond to parameters at the instability onset, and the circle symbols to those without the instability. The shaded area displays the region including square symbols for each configuration.

instability with collapse documented in this paper. As shown in Sec. I, the core $m/n = 2/1$ modes appear in a torus inward-shifted R_{ax} configuration ($R_{ax} < 3.60$ m). The locked-mode-like instabilities with the $m/n = 1/1$ structure appear in high aspect ratio configurations with co-plasma current, where the magnetic shear is low. The CDC events
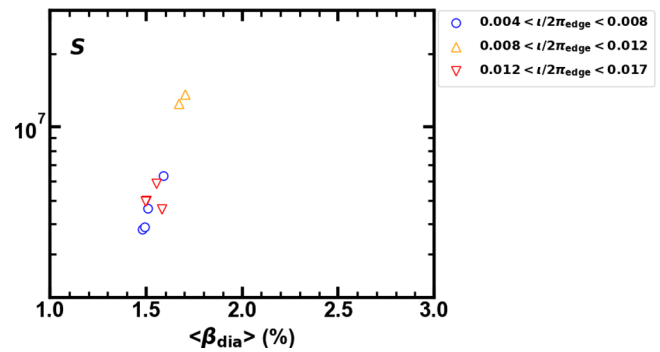
appear in a torus outward-shifted R_{ax} configuration ($R_{ax} > 3.75$ m). Furthermore, the edge $m/n = 1/1$ instabilities with collapse, which are documented in this paper, appear in a relatively low magnetic Reynolds number and medium beta regions. Figure 12(a) shows the degradation level of global confinement due to the collapse events as a function of the onset beta value. The degradation level due to the instabilities reported in this paper is comparable to that of the core instabilities with torus inward-shifted R_{ax} configurations, but smaller than that of the locked-mode-like instabilities. The onset beta value is comparable to that of the CDC events and the locked-mode-like instabilities, but smaller than that of the core instabilities with torus inward-shifted R_{ax} configurations.

Figure 12(b) shows the degradation level of global confinement due to the collapse events as the function of the onset magnetic Reynolds number, S. The onset S of the instabilities reported in this paper is much lower than those of the other collapse phenomena. It should be noted that the onset S of the locked-mode-like instabilities is higher than those of the other collapse phenomena. This is because the locked-mode-like instability is considered to be driven by an ideal interchange instability.[23]

VI. CONCLUSION AND DISCUSSION

The characteristics and the onset conditions of instabilities with plasma collapse observed in relatively high density and medium beta
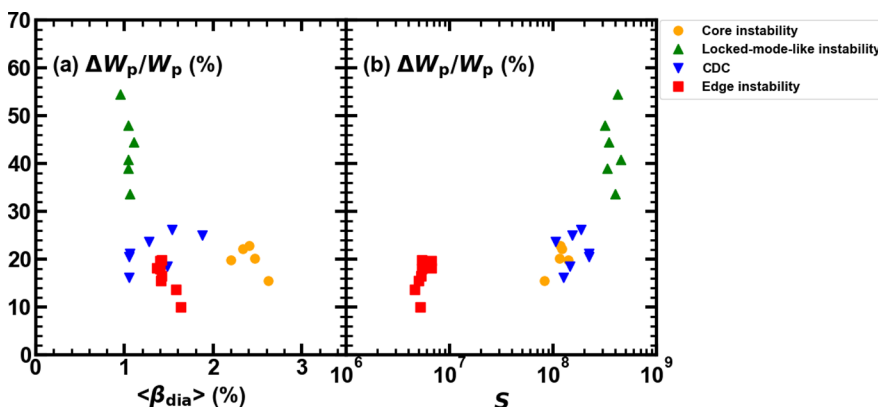

FIG. 12. The degradation level of global confinement due to the collapse events and (a) onset volume-averaged beta value and (b) onset magnetic Reynolds number of four types of MHD instabilities observed in the LHD. Red symbols (edge) correspond to instabilities reported in this paper.

regions, with the torus outward-shifted magnetic axis configuration of the LHD, are investigated. When beta value and the magnetic Reynolds number satisfy a specific condition, the $m/n = 1/1$ magnetic fluctuation rapidly grows and its frequency decreases, leading to beta reduction ($\sim$10%) due to core electron pressure inside the resonant surface. The frequency of the instability is smaller than that of the resistive interchange mode typically observed in the LHD. The instability has a radial structure with the odd parity around the resonant surface, which is similar to a tearing-type structure. The magnetic axis dependence of the onset conditions shows that the instabilities occur only in limited configurations with a magnetic axis of 3.65–3.775 m. In the configurations where the instability is absent, the resonant surface is apart from the location of a plasma boundary index, in which 99% of the volume-integrated electron pressure is contained. This result suggests that the distance between the resonant surface and the plasma boundary plays an important role in the instability onset, and a possibility that the instability with collapse reported in this paper is driven by an external mode.

ACKNOWLEDGMENTS

AUTHOR DECLARATIONS
Conflict of Interest

The authors have no conflicts to disclose.

Author Contributions

Yuki Takemura: Conceptualization (equal); Data curation (lead); Formal analysis (lead); Investigation (equal); Methodology (equal); Resources (equal); Visualization (lead); Writing – original draft (lead). **Kiyomasa Watanabe:** Conceptualization (equal); Investigation (equal); Methodology (equal). **Satoru Sakakibara:** Investigation (equal); Resources (equal). **Satoshi Ohdachi:** Investigation (equal); Resources (equal). **Yoshiro Narushima:** Resources (equal). **Kenji Tanaka:** Resources (equal). **Tokihiko Tokuzawa:** Resources (equal).

DATA AVAILABILITY

The data that support the findings of this study are available from the corresponding author upon reasonable request. The data that support the findings of this study are openly available in the LHD data repository at https://www-lhd.nifs.ac.jp/pub/Repository_en.html, Ref. 26.

APPENDIX: SUYDUM CRITERION

Here, the Suydum condition, which is a local stability criterion for an ideal interchange instability in cylindrical geometry, is considered. The Suydum criterion is written as follows:[24,25]

$$D_s \equiv \frac{-(R_0/r)^2(d\Omega/ds)(d\beta/ds)}{(d\iota/ds)^2} - \frac{1}{4} > 0, \qquad (A1)$$

where R_0 is the major radius at the magnetic axis, r is the minor radius, β is plasma beta value, Ω is curvature of the magnetic field and ι the rotational transform, s is toroidal magnetic flux normalized by that at the plasma boundary and the definition is $s \equiv \psi/\psi_e$, and $2\pi\psi$ is toroidal flux, and "e" corresponds to the plasma boundary. On the contrary, in the Boozer coordinates (ψ, θ, ζ), the s derivative of plasma volume is expressed by $\frac{dV}{ds} = \frac{d}{ds}\int \sqrt{g}d\psi d\theta d\zeta$, and Ω is defined as $\int \frac{B_0^2}{B^2}d\theta d\zeta$. Here, $\sqrt{g} \sim \frac{R_0 B_0}{B^2}$ is the Jacobian of the Boozer coordinate, B is the total magnetic field strength, and B_0 is the toroidal magnetic field strength at the magnetic axis. Then, the relation, $\frac{d\Omega}{ds} = \frac{B_0}{R_0\psi_e}\frac{dV}{ds}$, is obtained. By using the above relation, the Suydum condition is expressed as the following:

$$D_s = \frac{-\left(R_0 B_0/a_p^2\psi_e s\right)\left(d^2V/ds^2\right)}{(d\iota/ds)^2}\frac{d\beta}{ds} - \frac{1}{4} > 0, \qquad (A2)$$

where $r = \sqrt{s}a_p$ and a_p is the minor radius at the plasma boundary. The above equation means that the driving term of the ideal interchange instability is $-\left(R_0 B_0/a_p^2\psi_e s\right)\left(d^2V/ds^2\right)$, and the stabilizing term is $0.25(d\iota/ds)^2$ in cylindrical geometry. Thus, the comparison between the above two terms is reasonable in order to estimate the stability of the ideal interchange instability in a discharge with the same beta value and profile.

REFERENCES

[1]ITER Physics Expert Group on Disruptions, Plasma Control and MHD1 and ITER Physics Basis Editors, Nucl. Fusion **39**, 2251 (1999).

[2]T. C. Hender, J. C. Wesley, J. Bialek, A. Bondeson, A. H. Boozer, R. J. Buttery, A. Garofalo, T. P. Goodman, R. S. Granetz, Y. Gribov et al., Nucl. Fusion **47**, S128 (2007).

[3]M. Osakabe, H. Takahashi, H. Yamada, K. Tanaka, T. Kobayashi, K. Ida, S. Ohdachi, J. Varela, K. Ogawa, M. Kobayashi et al., Nucl. Fusion **62**, 042019 (2022).

[4]S. Sakakibara, H. Yamada, K. Y. Watanabe, Y. Narushima, K. Toi, S. Ohdachi, S. Yamamoto, K. Narihara, K. Tanaka, A. Komori et al., Plasma Phys. Controlled Fusion **44**, A217 (2002).

[5]A. Komori, H. Yamada, S. Sakakibara, O. Kaneko, K. Kawahata, T. Mutoh, N. Ohyabu, S. Imagawa, K. Ida, Y. Nagayama et al., Nucl. Fusion **49**, 104015 (2009).

[6]J. Miyazawa, R. Sakamoto, S. Ohdachi, M. Kobayashi, S. Masuzaki, T. Morisaki, S. Sakakibara, M. Goto, S. Morita, I. Yamada et al., Plasma Fusion Res. **3**, S1047 (2008).

[7]S. Ohdachi, R. Sakamoto, J. Miyazawa, T. Morisaki, S. Masuzaki, H. Yamada, K. Y. Watanabe, V. R. Jacobo, N. Nakajima, F. Watanabe et al., Contrib. Plasma Phys. **50**, 552 (2010).

[8]Y. Takemura, S. Sakakibara, Y. Narushima, M. Okamoto, K. Y. Watanabe, Y. Suzuki, S. Ohdachi, K. Ida, M. Yoshinuma, K. Tanaka et al., Nucl. Fusion **52**, 102001 (2012).

[9]Y. Takemura, K. Y. Watanabe, S. Sakakibara, S. Ohdachi, Y. Narushima, K. Ida, M. Yoshinuma, H. Tsuchiya, T. Tokuzawa, and I. Yamada, Nucl. Fusion **59**, 066036 (2019).

[10]Y. Takemura, K. Y. Watanabe, S. Sakakibara, S. Ohdachi, Y. Narushima, K. Ida, and M. Yoshinuma, Nucl. Fusion **61**, 026011 (2021).

[11]K. Y. Watanabe, Y. Suzuki, S. Sakakibara, T. Yamaguchi, Y. Narushima, Y. Nakamura, K. Ida, N. Nakajima, and H. Yamada, Fusion Sci. Technol. **58**, 160 (2010).

[12]S. P. Hirshman and J. C. Whitson, Phys. Fluids **26**, 3553 (1983).

[13]S. Sakakibara, K. Y. Watanabe, Y. Suzuki, Y. Narushima, S. Ohdachi, N. Nakajima, F. Watanabe, L. Garcia, A. Weller, K. Toi et al., Plasma Phys. Controlled Fusion **50**, 124014 (2008).

[14]S. Sakakibara and H. Yamada, Fusion Sci. Technol. **58**, 471 (2010).

[15]K. Tanaka, C. Michael, L. Vyacheslavov, A. Sanin, K. Kawahata, S. Okajima, T. Akiyama, T. Tokuzawa, and Y. Ito, Plasma Fusion Res. **2**, S1033 (2007).

[16]T. Tokuzawa, S. Inagaki, A. Ejiri, R. Soga, I. Yamada, S. Kubo, M. Yoshinuma, K. Ida, C. Suzuki, K. Tanaka et al., Plasma Fusion Res. **9**, 1 (2014).

[17]Y. C. Kim and E. J. Powers, Phys. Fluids **21**, 1452 (1978).

[18]K. Y. Watanabe, Y. Suzuki, T. Yamaguchi, K. Narihara, K. Tanaka, T. Tokuzawa, I. Yamada, S. Sakakibara, Y. Narushima, T. Morisaki et al., Plasma Phys. Controlled Fusion **49**, 605 (2007).

[19]Y. Narushima, K. Y. Watanabe, S. Sakakibara, N. Nakajima, K. Nishimura, H. Yamada, K. Yamazaki, W. A. Cooper et al., Proceedings of the 29th EPS Conference on Plasma Physics and Controlled Fusion Montreux, 17–21 June 2002 ECA 26B, P-1.080 (2002).

[20]Y. Narushima, S. Sakakibara, K. Y. Watanabe, K. Nishimura, H. Yamada, N. Nakajima, K. Yamazaki, W. A. Cooper et al., J. Plasma Fusion Res. **5**, 514 (2002).

[21]Y. Narushima, K. Watanabe, S. Sakakibara, and N. Nakajima, J. Plasma Fusion Res. **6**, 214 (2004).

[22]Y. Suzuki, K. Ida, K. Kamiya, M. Yoshinuma, S. Sakakibara, K. Y. Watanabe, and H. Yamada, Nucl. Fusion **53**, 073045 (2013).

[23]M. Okamoto, H. Tomita, K. Y. Watanabe, M. Sato, Y. Takemura, S. Sakakibara, K. Ida, and M. Yoshinuma, Nucl. Fusion **61**, 046005 (2021).

[24]B. R. Suydam, 1958 Peaceful Uses of Atomic Energy Proc. 2nd Int. Conf. (UN, Geneva, 1958) Vol. 31, p. 157.

[25]M. Wakatani, Stellarator and Heliotron Devices (Oxford University Press, 1998).

[26]See https://www-lhd.nifs.ac.jp/pub/Repository_en.html for large helical device project, LHD experiment data repository.